THE JOURNAL OF BIOLOGICAL CHEMISTRY
Vol. 276, No. 36, Issue of September 7, pp. 34189–34198, 2001
Printed in U.S.A.

Biophysical Characterization of Interactions Involving Importin-α during Nuclear Import*

Received for publication, April 20, 2001, and in revised form, July 9, 2001
Published, JBC Papers in Press, July 11, 2001, DOI 10.1074/jbc.M103531200

Bruno Catimel‡, Trazel Teh§¶, Marcos R. M. Fontes§‖, Ian G. Jennings§, David A. Jans, Geoffrey J. Howlett‡‡, Edouard C. Nice‡, and Bostjan Kobe§¶§§**

*From the ‡Ludwig Institute for Cancer Research, Royal Melbourne Hospital, Victoria 3050, the §Structural Biology Laboratory, St. Vincent's Institute of Medical Research, Fitzroy, Victoria 3065, the ¶Department of Biochemistry and Molecular Biology/Institute for Molecular Bioscience, University of Queensland, Brisbane, Queensland 4072, the **Nuclear Signaling Laboratory, Division for Biochemistry and Molecular Biology, John Curtin School of Medical Research, Australian National University, Canberra, ACT 2601, and the ‡‡Department of Biochemistry and Molecular Biology, University of Melbourne, Parkville, Victoria 3010, Australia*

Proteins containing the classical nuclear localization sequences (NLSs) are imported into the nucleus by the importin-α/β heterodimer. Importin-α contains the NLS binding site, whereas importin-β mediates the translocation through the nuclear pore. We characterized the interactions involving importin-α during nuclear import using a combination of biophysical techniques (biosensor, crystallography, sedimentation equilibrium, electrophoresis, and circular dichroism). Importin-α is shown to exist in a monomeric autoinhibited state (association with NLSs undetectable by biosensor). Association with importin-β (stoichiometry, 1:1; K_D = 1.1 × 10^{-8} M) increases the affinity for NLSs; the importin-α/β complex binds representative monopartite NLS (simian virus 40 large T-antigen) and bipartite NLS (nucleoplasmin) with affinities (K_D = 3.5 × 10^{-8} M and 4.8 × 10^{-8} M, respectively) comparable with those of a truncated importin-α lacking the autoinhibitory domain (T-antigen NLS, K_D = 1.7 × 10^{-8} M; nucleoplasmin NLS, K_D = 1.4 × 10^{-8} M). The autoinhibitory domain (as a separate peptide) binds the truncated importin-α, and the crystal structure of the complex resembles the structure of full-length importin-α. Our results support the model of regulation of nuclear import mediated by the intrasteric autoregulatory sequence of importin-α and provide a quantitative description of the binding and regulatory steps during nuclear import.

Nucleocytoplasmic transport occurs through nuclear pore complexes, large supramolecular structures that penetrate the double lipid layer of the nuclear envelope. Most macromolecules require an active, signal-mediated transport process that enables the passage of particles up to 25 nm in diameter (~25 MDa). The first and best characterized nuclear targeting signals are the classical nuclear localization sequences (NLSs)[1] that contain one or more clusters of basic amino acids (1). NLSs do not conform to a specific consensus sequence and fall into two distinct classes termed monopartite NLSs, containing a single cluster of basic amino acids, and bipartite NLSs, comprising two basic clusters.

Despite the sequence variability, the classical NLSs are recognized by the same receptor protein termed importin or karyopherin, a heterodimer of α and β subunits (for recent reviews see Refs. 2–6). Importin-α contains the NLS-binding site, and importin-β is responsible for the translocation of the importin-cargo complex through the pore. Transfer through the pore is facilitated by the proteins Ran (Ras-related nuclear protein) and nuclear transport factor-2. Once inside the nucleus, importin-β binds to Ran-GTP to effect the dissociation of the import complex; the importin subunits return to the cytoplasm separately and without the cargo. The directionality of nuclear import is thought to be conferred by an asymmetric distribution of the GTP- and GDP-bound forms of Ran between the cytoplasm and the nucleus. This distribution is in turn controlled by various Ran-binding regulatory proteins.

Importin-α consists of two structural and functional domains, a short basic N-terminal importin-β-binding (IBB) domain (7–9), and a large NLS-binding domain comprising armadillo (Arm) repeats (10). The monopartite NLSs bind at a major site located between the first and fourth Arm repeats and additionally at a minor site spanning repeats 4–8 (11–13). The bipartite NLSs span the two binding sites, with each site recognizing one of the basic clusters (12, 13). The linker sequence between the two basic clusters makes few contacts with the receptor, consistent with its tolerance to mutations. The affinity of the importin-targeting sequence interaction is a critical parameter in determining transport efficiency (3).

The structure of mouse importin-α showed that in the absence of importin-β or NLS-containing proteins, a part of the IBB domain occupies the major NLS-binding site (14). Based on this observation, it was suggested that the IBB domain acts as an intrasteric autoregulatory sequence (15), explaining the regulatory switch between the cytoplasmic, high affinity form and the nuclear, low affinity form for NLS binding (14). This model is supported by the observed increase in affinity for NLSs of importin-α upon importin-β binding (16–19).

* This work was supported in part by funds from the Wellcome Trust and the National Health and Medical Research Council (to B. K.). The costs of publication of this article were defrayed in part by the payment of page charges. This article must therefore be hereby marked "*advertisement*" in accordance with 18 U.S.C. Section 1734 solely to indicate this fact.

‖ Supported by the Fundação de Amparo à Pesquisa do Estado de São Paulo, Brazil. Permanent address: Dept. de Física e Biofísica, Instituto de Biociências, UNESP, Caixa Postal 510, 18618-000, Botucatu/SP, Brazil.

§§ Wellcome Senior Research Fellow in Medical Science in Australia. To whom correspondence should be addressed.

[1] The abbreviations used are: NLS, nuclear localization sequence; Arm, armadillo; IBB domain, importin-β-binding domain (importin-α residues 1–70); Impα(70–529), importin-α lacking the N-terminal 69 residues; NHS/EDC, *N*-hydroxysuccinimide/*N*-ethyl-*N*′-(3-diethylaminopropyl)-carbodiimide; T-Ag, SV40 large T-antigen; GST, glutathione *S*-transferase; RU, resonance unit(s); ELISA, enzyme-linked immunosorbent assay.

In this study we use a combination of biophysical techniques to characterize the various binding and regulatory events occurring during nuclear import. The association state of individual importin subunits and the complex is characterized by sedimentation equilibrium and gel electrophoresis, the interactions involving importin-α are characterized using the biosensor, and the structure of the IBB/autoinhibitory domain and its interaction with the Arm repeat domain of importin-α are analyzed by x-ray crystallography and circular dichroism spectroscopy. Our experiments support the model of regulation of nuclear import mediated by the intrasteric autoregulatory sequence in importin-α and provide a quantitative description of the binding steps involving importin-α during nuclear import.

EXPERIMENTAL PROCEDURES

Protein Expression and Purification—Full-length, N-terminally truncated (comprising residues 70–529; Impα(70–529)) and the IBB domain (comprising residues 1–70) of mouse importin-α (α2 isoform) (20) and mouse importin-β (β1) were expressed recombinantly as fusion proteins containing an N-terminal glutathione *S*-transferase (GST) tag in *Escherichia coli* and purified by affinity chromatography using glutathione-Sepharose. The full-length pGEX-2T/importin-α and pGEX-2T/importin β clones were described previously (21). Truncated importin α and IBB domain constructs were generated by polymerase chain reaction using the pET30a construct containing the full-length importin α gene (22) as the template, and the following primer pairs: Impα(70–529), forward, 5′-GGAAAAC**GGATCC**AACCAGGGTACTG-3′, and reverse, 5′-CGAC**GAATTC**TTAGAAGTTAAAGGT-3′; IBB domain, forward, 5′-CCGG**GGATCC**ATGTCCACGAACGAG-3′, and reverse, 5′-GTTAC**GAATTC**TTAGTTGTTCCGGTTTTC-3′ (restriction sites are in bold type). Polymerase chain reaction products were ligated into the *Bam*HI/*Eco*RI sites of pGEX-2T (Amersham Pharmacia Biotech), and the plasmids were transformed into BL21(DE3) *E. coli* cells. For expression, bacteria were grown at 37 °C to an A_{600} of 1.2 and induced with 1 mM isopropyl-1-thio-β-D-galactopyranoside. GST-free proteins were generated by thrombin cleavage (23). Prior to biosensor, circular dichroism, and sedimentation equilibrium experiments, the proteins were further purified by size exclusion chromatography using a Superdex 200 column (Amersham Pharmacia Biotech). The Impα(70–529) protein used for crystallization experiments was expressed as a hexahistidine-tagged protein and purified as described previously (13).

Peptide Synthesis—The peptides PKKKRKV (T-Ag NLS, corresponding to the NLS of the SV40 large T-antigen, residues 126–132) and KRPAATKKAGQAKKKK (nucleoplasmin NLS, corresponding to the NLS of nucleoplasmin, residues 155–170) with an N-terminal biotin group, and the peptide DEQMLKRRNVS (corresponding to residues 44–54 of mouse importin-α) were synthesized using the Applied Biosystems 433A peptide synthesizer, purified by cation exchange chromatography followed by reverse phase chromatography, and analyzed by quantitative amino acid analysis (Beckman 6300 amino acid analyzer) and electrospray mass spectrometry (Sciex API 111; PerkinElmer Life Sciences) (24).

Biosensor Analysis—The protein concentration was determined by absorbance at 280 nm as calculated from the amino acid composition (ProtParam). Protein homogeneity was checked prior to kinetic studies using micropreparative size exclusion chromatography (Superose 12 column HR 3.2/30) connected to a SMART system (Amersham Pharmacia Biotech). All measurements were performed using a BIAcore2000 biosensor (BIAcore AB). Importin-α, importin-β, IBB domain, and anti-GST IgG were immobilized onto a carboxymethyldextran sensor chip using NHS/EDC coupling as described previously (25). GST-importin-β and GST-IBB were captured onto immobilized anti-GST IgG, and biotinylated NLS peptides were immobilized onto streptavidin-coated surfaces according to protocols described previously (26, 27). The samples for analyses were prepared at various concentrations in HBS buffer (10 mM Hepes, pH 7.4, containing 3.4 mM EDTA, 0.15 mM NaCl, and 0.005% (v/v) Tween 20) and were injected (30 μl) over the sensor surface at a flow rate of 10 μl min^{-1}. Following completion of the injection phase, dissociation was monitored in HBS buffer for 150 s at the same flow rate. Bound proteins were eluted, and the surface was regenerated between injections, using either 30 μl of 10 mM HCl or 10 mM NaOH. Regeneration conditions did not denature the immobilized antigen as shown by equivalent signals upon reinjection of the ligand.

The apparent association and dissociation rate constants were calculated using BIAevaluation version 3.0 (BIAcore AB) as described previously (28). The goodness of the fit between experimental data and fitted curves was estimated from the coefficient of correlation, R^2 (for linear fitting routines), or by χ^2 analysis using the following equation (for nonlinear least squares fitting, see Tables I and II).

$$\chi^2 = \frac{{}_1\Sigma^n(r_f - r_x)^2}{n - p} \qquad \text{(Eq. 1)}$$

Sedimentation Equilibrium—Sedimentation equilibrium experiments were performed using Beckman XL-A analytical ultracentrifuge equipped with a Ti60 rotor and filled-epon centerpieces (path length, 12 mm). Sedimentation equilibrium profiles for importin-α and importin-β at starting concentrations of 0.5 mg ml^{-1} were obtained at 20 °C, using rotor speeds of 10,000 and 15,000 rpm. The final equilibrium distributions, determined from absorption measurements at 280 nm, were fitted globally to obtain best fit values for the molecular weight. The complex formed between importin-α and importin-β was isolated by size exclusion chromatography (Superose 200; Amersham Pharmacia Biotech) and sedimentation equilibrium distributions obtained at 20 °C, using a rotor speed of 10,000 rpm. Partial specific volumes for importin-α and importin-β (0.74 ml g^{-1}) were calculated from the amino acid composition; the solvent density of S buffer (10 mM sodium phosphate, 1.8 mM potassium phosphate, 2.7 mM KCl, 0.2 M NaCl, pH 7.3) was calculated to be 1.007 g ml^{-1}.

Circular Dichroism Spectroscopy—Spectra of the IBB domain were recorded at 20 °C using the IBB domain at a concentration of 0.108 mg ml^{-1} in 20 mM sodium phosphate buffer (pH 7), with an Aviv model 62DS spectrophotometer, 1-mm path-length quartz cuvettes, 1.5 nm bandwidth, 2 s integration time, and 0.5 nm wavelength increments from 185 to 260 nm. The spectra were corrected with a base line obtained using buffer alone under the same conditions.

Crystal Structure Determination—For crystallization, Impα(70–529) was concentrated to 18.8 mg ml^{-1} using a Centricon-30 (Millipore) and stored at −20 °C. Crystallization conditions were screened by systematically altering various parameters using the crystallization conditions for other peptide complexes (13) as a starting point. The crystals (rod shaped, 0.3 × 0.1 × 0.07 mm) were obtained using co-crystallization, by combining 2 μl of protein solution, 1 μl of peptide solution (1.7 mg ml^{-1}; peptide/protein ratio, 2.5), and 2 μl of reservoir solution and suspended over 0.5 ml of reservoir solution containing 0.6 M sodium citrate as the precipitant (pH 6.5) and 10 mM dithiothreitol. The crystals exhibited orthorhombic symmetry (space group $P2_12_12_1$; see Table III). Diffraction data were collected from single crystals transiently soaked in a solution corresponding to the reservoir solution but supplemented with 23% glycerol and flash cooled at 100 K in a nitrogen stream (Oxford Cryosystems), using a MAR Research image plate detector (plate diameter, 345 mm) and CuKα radiation from a Rigaku RU-200 rotating anode generator. The data were auto-indexed and processed with the HKL suite (29) (see Table III).

The crystals were highly isomorphous with the crystals of full-length importin-α (14); therefore this structure (Protein Data Bank code 1IAL) with N-terminal residues omitted was used as a starting model for crystallographic refinement. Electron density maps were inspected for the presence of the peptide after rigid body refinement using the program CNS (30) (R_{cryst} = 30.5%; R_{free} = 31.2%; resolution, 6–3.5 Å; see Table III for explanation of *R* factors), and the model of the peptide was added. Electron density maps calculated with coefficients $3|F_{obs}| - 2|F_{calc}|$ and simulated annealing omit maps (see Fig. 5) calculated with analogous coefficients were generally used. The model was improved, as judged by the free *R* factor (31), through rounds of crystallographic refinement (positional and restrained isotropic individual B factor refinement, with an overall anisotropic temperature factor and bulk solvent correction), and manual rebuilding (program O) (32). Solvent molecules were added with the program CNS (30). Asn^{239} is an outlier in the Ramachandran plot as also observed in all other structures of mouse importin-α (13, 14). Pro^{242} is a *cis*-proline. The final models comprise 426 importin-α residues (residues 72–497) and 16 peptide residues. The structure determination statistics are shown in Table III. The coordinates have been deposited in the Protein Data Bank (code 1IQ1).

The quality of the models was checked with the program PROCHECK (33). The contacts were analyzed with the program CONTACT (34), and the buried surface areas were calculated using the program CNS (30).

RESULTS

Oligomeric States of Importin-α, Importin-β, and Their Complex—Sedimentation equilibrium analysis was used to deter-

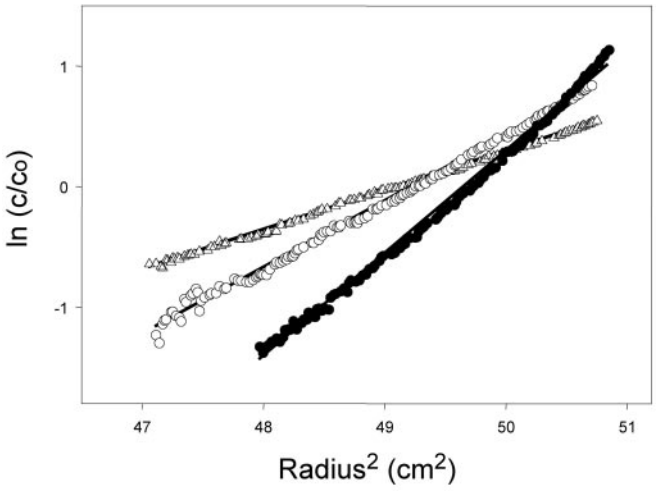

FIG. 1. **Sedimentation equilibrium profiles for importin-α, importin-β, and the importin-α/β complex.** The solutions in S buffer were centrifuged at 10,000 rpm and 20 °C for 16 h. The equilibrium profiles are presented as $\ln(c/c_o)$ *versus* the square of the radial distance, where c/c_o is the optical density at 280 nm divided by the initial optical density. For a single species, the slope of this plot is proportional to the molecular weight. *Triangles*, importin-α, initial concentration 0.5 mg ml^{-1}; *empty circles*, importin-β, initial concentration 0.5 mg ml^{-1}; *filled circles*, importin-α/β complex obtained from gel filtration, initial optical density of 0.44 mg ml^{-1}.

mine the oligomeric state of purified importin-α and importin-β (Fig. 1). The linearity of the ln*c versus* r^2 plots (*c* is the optical density at 280 nm, and *r* is the radial distance) for both proteins indicate single sedimenting species. Global analysis of sedimentation equilibrium data obtained at 10,000 and 15,000 rpm gives values for the molecular weights of importin-α and importin-β of 60,100 and 99,000, respectively. These values correspond closely to the subunit molecular weights of importin-α (60,294) and importin-β (97,130), suggesting that both proteins are monomeric under these conditions. The complex formed between importin-α and importin-β was isolated as a single major peak from gel filtration chromatography. Sedimentation equilibrium analysis of this sample (Fig. 1) indicated minor molecular weight heterogeneity represented by the deviations from linearity. The slope of the straight line drawn through the data yields an estimate for the weight average molecular weight of the complex of 148,200, consistent with a 1:1 complex. The stoichiometry of binding was further analyzed by gel electrophoresis, by comparing the relative intensities of the protein bands of the complex, as isolated by size exclusion chromatography, with the relative intensities of importin-α and -β mixed in varying ratios; these experiments also suggested 1:1 stoichiometry of binding (data not shown).

Biosensor Analysis of the Importin-α-Importin-β Interaction—Surface plasmon resonance was used to characterize the apparent association (k_a) and dissociation (k_d) constants of the importin-α-importin-β interaction. Initially, importin-β was covalently linked to the flexible dextran matrix of a carboxymethyldextran sensor chip via amine coupling (~9,000 resonance units (RU) corresponding to 9 ng mm^{-2}) (35). However, the resulting surface gave only a weak nonspecific signal upon importin-α injection, even at concentrations up to 1 μM (data not shown). This suggested that importin-β was not immobilized in an active orientation for importin-α binding. To attain an optimal presentation for importin-α binding, GST-tagged importin-β was captured onto the sensor chip using an immobilized anti-GST antibody. Because the GST-importin was desorbed during regeneration, this required reloading the surface prior to each analysis. The amount of importin-β captured at

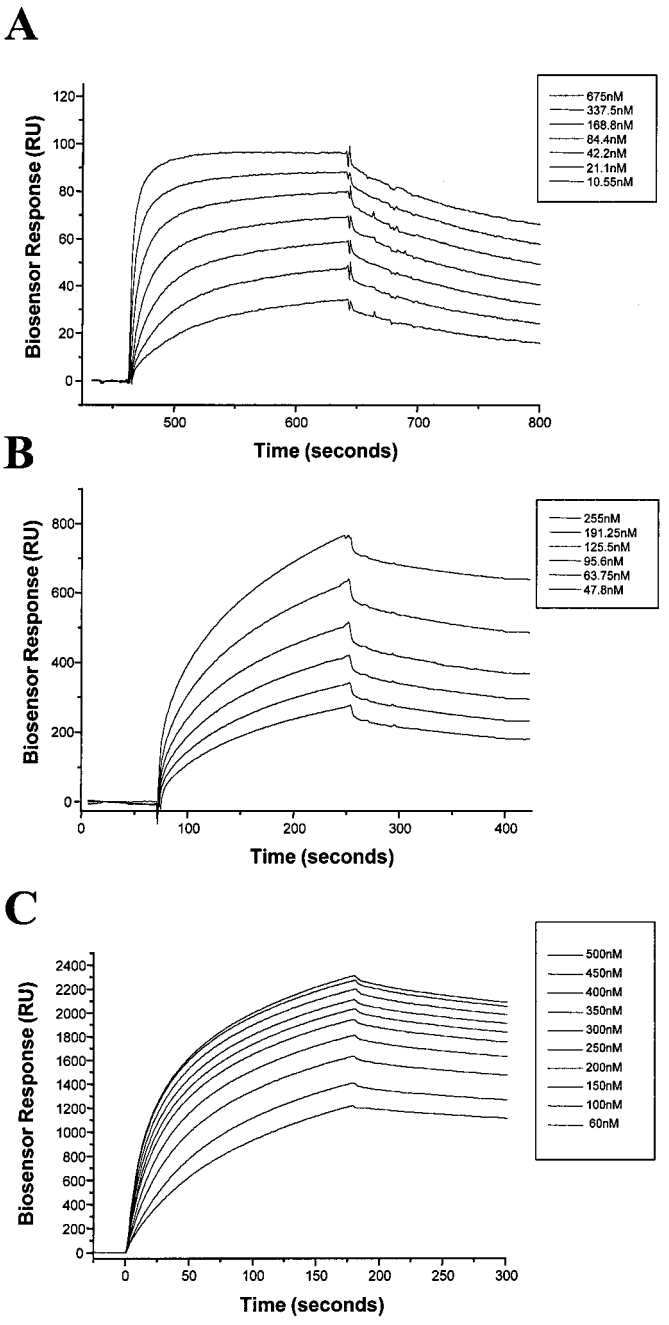

FIG. 2. **Biosensor analysis of importin-α/β interaction.** *A*, varying concentrations of importin-α (675–10.55 nM) were injected over GST-importin-β captured using immobilized anti-GST-IgG. *B*, varying concentrations of importin-β (255–47.8 nM) were injected over importin-α immobilized via NHS/EDC. *C*, varying concentrations of importin-β (500–60 nM) were injected over GST-IBB domain captured using immobilized anti-GST-IgG.

each cycle was ~500 RU, varying from 525 RU at the first injection to 485 RU after 10 injections. This small variation in captured antigen was probably due to a minor loss of reactivity of the immobilized anti-GST antibody (IgG) upon regeneration between cycles.

This slight difference in surface levels between cycles precluded global analysis for this data set, with each curve having to be analyzed separately using nonlinear least squares regression analysis. The binding curves (Fig. 2*A*) fitted poorly using the simple 1:1 Langmuirien model (A + B ⇄ AB), suggesting complex kinetics. This was not unexpected considering the available structural information; the IBB domain needs to dissociate from the Arm repeat domain of importin-α before bind-

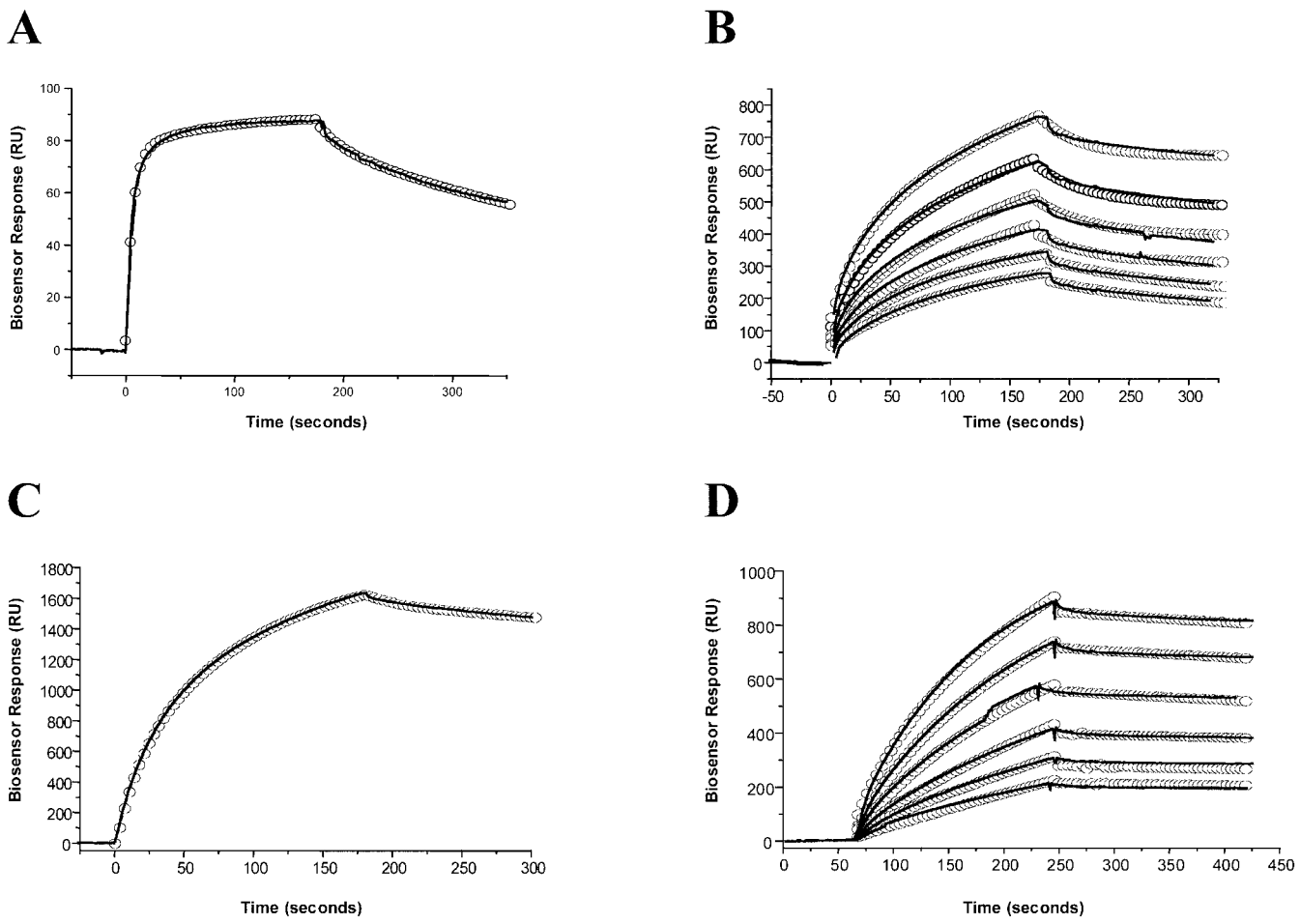

FIG. 3. **Analysis of the BIAcore binding data.** The experimental data are indicated by *solid lines*, and the fitted data are indicated by *open circles*. *A*, binding of importin-α (168.8 nM) over GST-importin-β captured by an anti-GST IgG (nonlinear least squares regression analysis with a two-state reaction conformational change model). *B*, binding of importin-β (255–47.8 nM) over importin-α immobilized via NHS/EDC (global analysis with a two-state reaction conformational change model). *C*, binding of importin-β (150 nM) over GST-IBB captured by an anti-GST IgG (nonlinear least squares regression analysis with a two-state reaction conformational change model). *D*, binding of Imp-α(70–529) (460–86.5 nM) over immobilized nucleoplasmin NLS peptide (global analysis with a 1:1 Langmuirien model).

ing importin-β, simultaneously undergoing conformational changes upon importin-β binding (14, 36, 37). Therefore, a two-state reaction model appeared appropriate for the analysis of the binding curves. This model gave an excellent fit (Fig. 3*A*) compared with other models tested. The analysis of each individual curve, generated using a range of concentrations (337.5–5.25 nM) gave similar results (values ranging from $3.9–6.6 \times 10^5$ M^{-1} s^{-1} for k_{a1}, $1.5–1.9 \times 10^{-2}$ s^{-1} for k_{d1}, $6.7–8.4 \times 10^3$ M^{-1} s^{-1} for k_{a2}, and $2.1–3.2 \times 10^{-3}$ s^{-1} for k_{d2}) resulting in an apparent $k_{a1} = 4.9 \times 10^5$ M^{-1} s^{-1}, $k_{d1} = 1.7 \times 10^{-2}$ s^{-1} (for the reaction A + B ⇄ AB), and $k_{a2} = 7.9 \times 10^3$ M^{-1} s^{-1}, and $k_{d2} = 2.5 \times 10^{-3}$ s^{-1} (for the rearrangement AB ⇄ AB*). These values resulted in an apparent dissociation constant $K_D = 1.1 \times 10^{-8}$ M (Table I).

The binding was also analyzed in the reverse orientation (importin-β injected over immobilized importin-α). The immobilization was performed using amine chemistry coupling onto a carboxymethyldextran surface (0.7 ng mm^{-2} immobilized). This yielded an active surface as shown by importin-β binding (Fig. 2*B*). Again, the two-state reaction model could be used to analyze this interaction, and global fitting could be used because the binding surface was stable (Fig. 3*B*). Apparent association and dissociation rate constants determined for this interaction were: $k_{a1} = 8.7 \times 10^4$ M^{-1} s^{-1}, $k_{d1} = 1.4 \times 10^{-2}$ s^{-1} (for the reaction A + B ⇄ AB), and $k_{a2} = 35 \times 10^3$ M^{-1} s^{-1}, $k_{d2} = 4.9 \times 10^{-4}$ s^{-1} (for the rearrangement AB ⇄ AB*), resulting in a dissociation constant $K_D = 1.4 \times 10^{-8}$ M (Table I). This is in excellent agreement with the reverse orientation experiments (Table I). The binding of truncated importin-α (70–529), which lacks the IBB domain, to GST-captured importin-β was used as a control; no binding was observed.

The N-terminal IBB domain of importin-α has been shown to be necessary and sufficient for importin-β binding (7, 36). To investigate quantitatively whether the isolated IBB domain had similar binding properties to that of intact importin-α to importin-β, we expressed the N-terminal 70 residues of importin-α as a GST fusion protein and also generated the nontagged protein by proteolytic cleavage. Immobilization of the nontagged IBB domain using amine coupling resulted in an inactive surface for importin-β binding; this was not unexpected because several lysine residues of the IBB domain are within or close to the importin-β-binding site (36). The IBB domain bound importin-β that was immobilized using the amine chemistry (data not shown), in contrast to full-length importin-α; these data suggest that the isolated binding domain may have better access to the binding site compared with the larger intact importin-α molecule. However, the curves displayed complex kinetics that could not be readily fitted by any available model; visually the curves appeared to comprise initial fast apparent on and off rate constants. A similar interaction was observed when binding the IBB domain to GST-importin-β immobilized via the anti-GST antibody (data not shown). We

TABLE I
Analysis of binding constants using nonlinear least squares and global fitting with a two-state conformational change model

Immobilized ligand	Soluble ligand	Analysis	k_{a1}	k_{a2}	k_{d1}	k_{d2}	K_D
			$\times 10^5\ M^{-1}\ s^{-1}$	$\times 10^3\ M^{-1}\ s^{-1}$	$\times 10^{-2}\ s^{-1}$	$\times 10^{-4}\ s^{-1}$	$\times 10^{-8}\ M$
Importin-β (GST)	importin-α	NLLS (conformational change)[a]	4.9	7.9	1.7	25	1.1
Importin-α (amino)	importin-β	global fitting (conformational change)	0.9	35	1.4	4.9	1.4
IBB domain (GST)	importin-β	NLLS (conformational change)	1.1	24	2.4	7.4	0.7
T-Ag NLS (amino)	importin-α/β	global fitting (conformational change)	1.5	6.4	7.5	4.4	3.5
Nucleoplasmin NLS (amino)	importin-α/β	global fitting (conformational change)	1.3	4.7	3.5	8.4	4.8

[a] NLLS, nonlinear least square.

therefore resorted to immobilizing the GST-IBB domain fusion protein via the anti-GST antibody and analyzing the binding of importin-β (Fig. 2*C*). The amount of GST-IBB captured at each cycle varied slightly from 725 RU at the first injection to 650 RU at the last injection. Again, because of this variation in surface immobilization, nonlinear least square fitting was performed on individual curves using the conformational change model (Fig. 3*C*). The analysis gave an apparent $k_{a1} = 1.1 \times 10^5$ M^{-1} s^{-1}, $k_{d1} = 2.4 \times 10^{-2}$ s^{-1} (for the reaction A + B ⇄ AB), and $k_{a2} = 2.4 \times 10^{-2}$ M^{-1} s^{-1}, $k_{d2} = 7.4 \times 10^{-4}$ s^{-1} (for the rearrangement AB ⇄ AB*). These values result in an apparent dissociation constant $K_D = 7 \times 10^{-9}$ M (Table I).

In the crystal structure of importin-α, residues 44–54 interact with the Arm repeat domain (residues 70–529) of the protein, presumably autoinhibiting the receptor. We examined the binding of the IBB domain to immobilized N-terminally truncated importin-α (Impα(70–529)). Binding could be observed between the two domains, although the low affinity and complex binding kinetics comprising very fast on and off rates prevented a rigorous analysis of this interaction using the biosensor (results not shown). The dissociation constant could be estimated at ~4×10^{-6} M.

Biosensor Analysis of Importin Binding to NLS Peptides—To analyze the interaction of importin-α with representative NLSs from the two major classes, monopartite and bipartite NLSs, the peptides corresponding to the monopartite NLS from SV40 large T-antigen (T-Ag NLS) and the bipartite NLS from nucleoplasmin were immobilized via an N-terminal biotin group to a streptavidin-coupled sensor chip surface (~0.6 and 0.43 ng mm^{-2} of T-Ag and nucleoplasmin NLS, respectively, were immobilized). Initially, the binding of the N-terminally truncated protein Impα(70–529) (which lacks the autoinhibitory domain) was investigated (Fig. 4, *A* and *B*). The curves were analyzed using a 1:1 Langmuirien model (the simultaneous binding of two immobilized monopartite NLS peptides to the major and minor sites of the same importin-α molecule is unlikely) (Fig. 3*D* and Table II). Both the monopartite and bipartite NLS had similar apparent association and dissociation rates, resulting in a dissociation constant $K_D = 1.5 \times 10^{-8}$ M for both peptides.

The binding of full-length importin-α to the immobilized NLS peptides was then tested. No binding could be detected under the experimental conditions tested (Fig. 4, *C* and *D*), in agreement with the proposed autoinhibitory effect of the residues 44–54 within the IBB domain. Because importin-α is autoinhibited in the absence of importin-β, the predominant NLS-binding form *in vivo* is likely to be the importin-α/β complex rather than importin-α alone. The importin-α/β complex was generated by mixing the proteins in a 1:1 ratio. Analytical centrifugation, gel electrophoresis, and size exclusion chromatography had shown previously that this formed a 1:1 complex. This complex was passed over the sensor chip containing the immobilized NLS peptides. In contrast to full-length importin-α alone, the importin-α/β complex bound well to immobilized NLS sequences (Fig. 4, *E* and *F*). The binding curves displayed complex kinetics and could not be described by the 1:1 Langmuirien model. To estimate the kinetic constants of this interaction, we assumed, based on the sedimentation (Fig. 1) and size exclusion data, that the importin-α/β complex was a single entity binding to the immobilized NLS peptide. With this assumption, the binding curves were again best fitted using the two state model (A + B = AB ⇄ AB*). The apparent association and dissociation rates are shown in Table I. The resulting dissociation constants were $K_D = 3.5 \times 10^{-8}$ M and $K_D = 4.8 \times 10^{-8}$ M for T-Ag and nucleoplasmin NLS, respectively.

Crystal Structure of the Impα(44–54)-Impα(70–529) Complex—The crystal structure of full-length mouse importin-α revealed electron density in the major NLS-binding site that was interpreted as residues 44–54 in the N-terminal region of the protein (14). No interpretable density was present for residues 55–69 linking this region with the Arm repeat domain. To confirm our interpretation of the electron density, we determined the crystal structure of the N-terminally truncated protein Impα(70–529) co-crystallized with a peptide corresponding to residues 44–54 of importin-α. The co-crystals grew in similar conditions and isomorphously to the native importin-α (13, 14) (Table III). Electron density maps based on the importin-α model, following rigid body refinement, clearly showed electron density corresponding to the peptide. The structure was refined at 2.8 Å resolution (Table III). The structure of Impα(70–529) is essentially identical to the corresponding portion of the full-length importin-α (the root mean square deviation of Cα atoms of residues 72–496 is 0.27 Å between full-length importin-α and the Impα(44–54)-Impα(70–529) complex). As observed for the monopartite T-Ag NLS (11, 13), two peptides bound to one molecule of importin-α. This contrasts full-length importin-α, most likely because the linker sequence 55–69 prevents the autoinhibitory sequence from reaching into the minor site and is attributable to the excess of the peptide relative to the Impα(70–529) protein in the co-crystallization experiments. Residues 45–53 and 47–53 of the peptide in the major site and minor site, respectively, could unambiguously be interpreted in the electron density map. The binding in the major site shows a similar binding mode of the peptide to the Arm repeat region of importin-α as observed in the native protein (14), confirming the original interpretation of the electron density of the native protein (root mean square deviation of Cα atoms of residues 49–53 is 0.06 Å between full-length importin-α and the Impα(44–54)-Impα(70–529) complex) (Fig. 5). The N-terminal

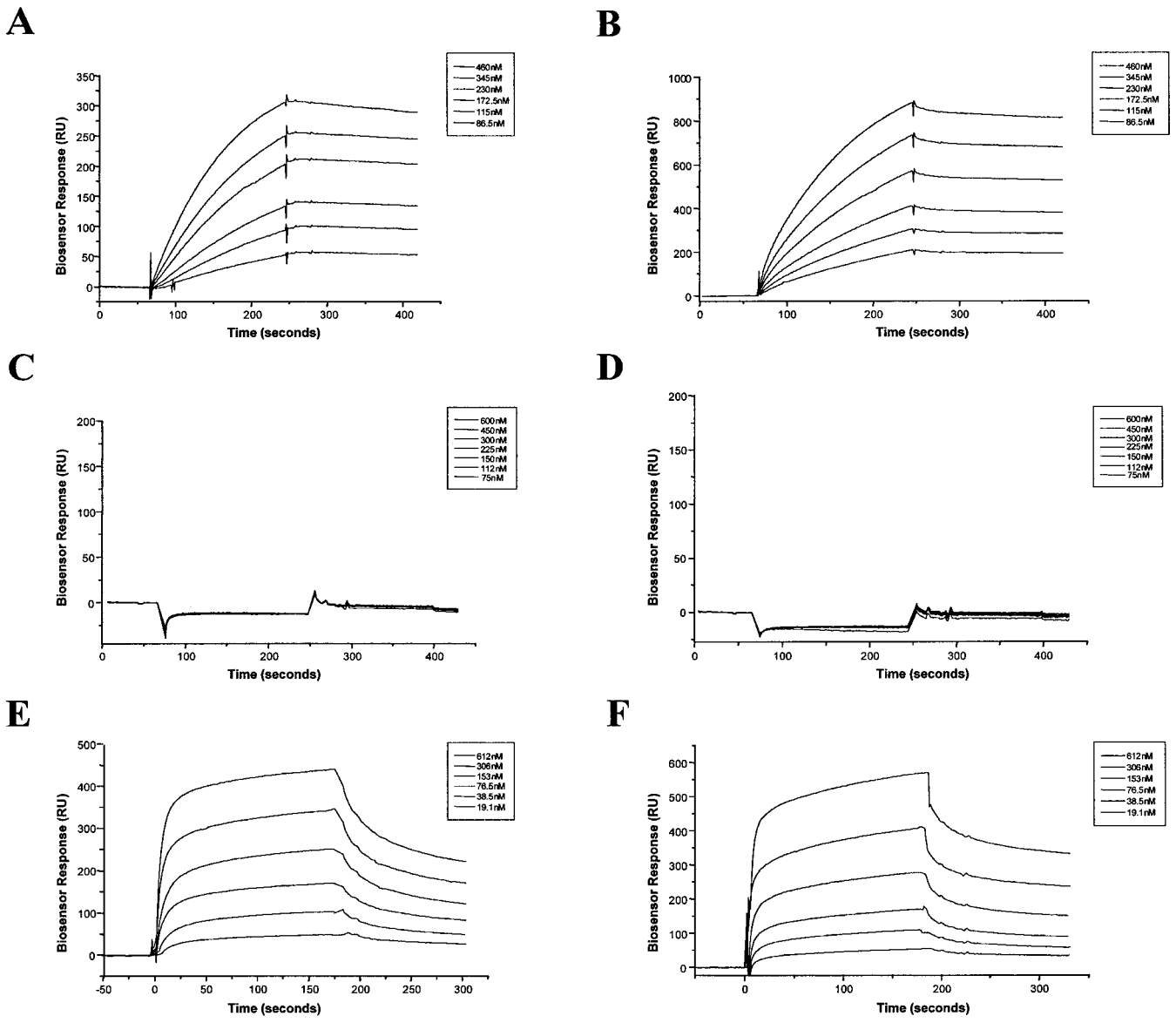

FIG. 4. **Biosensor analysis of importin-NLS interaction.** Biotinylated T-Ag and nucleoplasmin NLS were immobilized onto a streptavidin surface. *A*, Varying concentrations of Imp-α(70–529) (460–86.5 nM) were injected over immobilized T-Ag NLS. *B*, varying concentrations of Imp-α(70–529) (460–86.5 nM) were injected over immobilized nucleoplasmin NLS. *C*, varying concentrations of importin-α (full-length) (600–75 nM) were injected over immobilized T-Ag NLS. *D*, varying concentrations of importin-α (full-length) (600–75 nM) were injected over immobilized nucleoplasmin NLS. *E*, varying concentrations of importin-α/β complex (612–19.1 nM) were injected over immobilized T-Ag NLS. *F*, varying concentrations of importin-α/β complex (612–19.1 nM) were injected over immobilized nucleoplasmin NLS.

TABLE II
Analysis of binding constants using nonlinear least squares and global fitting with a Langmuirien model

Immobilized ligand	Soluble ligand	Analysis	k_a	k_d	K_D
			$\times 10^4\ M^{-1}\ s^{-1}$	$\times 10^{-4}\ s^{-1}$	$\times 10^{-8}\ M$
T-Ag NLS	Impα(70–529)	NLLS:Langmuir[a]	2.0	3.1	1.55
		Global fitting:Langmuir	1.95	3.3	1.69
Nucleoplasmin NLS	Impα(70–529)	NLLS:Langmuir	2.1	3.0	1.5
		Global fitting:Langmuir	1.6	2.2	1.4

[a] NLLS, nonlinear least square.

residues 45–48 superimpose less closely with the corresponding residues of the full-length importin-α (root mean square deviation of Cα atoms is 0.39 Å), possibly revealing the influence of the N-terminal residues not present in the peptide.

Structure of the IBB Domain of Importin-α—The IBB domain of importin-α is largely mobile as observed in the crystal structure of mouse importin-α, except for residues 44–54 that are bound in an extended conformation to the major NLS binding site of the protein (14). The same domain is involved in binding to importin-β, where it adopts a largely helical conformation (36). We therefore tested the inherent conformational propensity of this domain removed from the context of importin-α or importin-β proteins, using circular dichroism spectroscopy. In a physiological buffer, the domain shows little secondary struc-

TABLE III
Crystal structure determination

Diffraction data statistics	
Unit cell dimensions (Å)	
a	78.9
b	89.6
c	100.4
Resolution (Å)	30–2.8 (2.9–2.8)[a]
Observations	142,209
Unique reflections	18,165
Completeness (%)	97.6 (96.9)[a]
R_{merge} (%)[b]	12.4 (56.1)[a]
Average I/σ(I)	8.9 (1.3)[a]
Refinement statistics	
Resolution (Å)	30–2.8 (2.9–2.8)[a]
Number of reflections ($F > 0$)	17,671 (2,755)[a]
Completeness (%)	97.6 (97.8)[a]
R_{cryst} (%)[c]	20.9 (31.5)[a]
R_{free} (%)[d]	24.8 (33.5)[a]
Number of nonhydrogen atoms	
Protein	3,244
Peptide	136
Water	95
Mean B-factor (Å^2)	51.6
Root mean square deviations from ideal values[e]	
Bond lengths (Å)	0.007
Bond angles (°)	1.2
Ramachandran plot[f]	
Residues in most favored (disallowed) regions (%)	92.5 (0.3)
Coordinate error (Å)[e]	
Luzzati plot (cross-validated Luzzati plot)	0.34 (0.39)
SIGMAA (cross-validated SIGMAA)	0.45 (0.47)

[a] Numbers in parenthesis are for the highest resolution shell.
[b] $R_{merge} = \Sigma_{hkl} (\Sigma_i |I_{hkl,i} - \langle I_{hkl}\rangle|)/\Sigma_{hkl,i} \langle I_{hkl}\rangle$, where $I_{hkl,i}$ is the intensity of an individual measurement of the reflection with Miller indices h, k, and l, and $\langle I_{hkl}\rangle$ is the mean intensity of that reflection. Calculated for $I > -3\sigma(I)$.
[c] $R_{cryst} = \Sigma_{hkl} (||F_{obs hkl}| - |F_{calc hkl}||)/|F_{obs hkl}|$, where $|F_{obs hkl}|$ and $|F_{calc hkl}|$ are the observed and calculated structure factor amplitudes, respectively.
[d] R_{free} is equivalent to R_{cryst} but calculated with reflections (5%) omitted from the refinement process.
[e] Calculated with the program CNS (30).
[f] Calculated with the program PROCHECK (33).

ture, suggesting a flexible domain that can easily adapt to the context of the binding protein (Fig. 6).

DISCUSSION

Importin-α-Importin-β Binding—Although the importin subunits have been reported to associate with 1:1 stoichiometry (38), the oligomeric state of the individual subunits and the complex has not previously been rigorously examined. We used sedimentation equilibrium and gel electrophoresis to determine the association state of these proteins and show that the two monomeric proteins associate in a 1:1 complex. The observation of the monomeric state of importin-α is significant for several reasons. Firstly, the crystal structure and dynamic light scattering of N-terminally truncated yeast importin-α showed a dimeric molecule and prompted the authors to suggest an autoregulatory mechanism involving dimerization (11); dimerization was also implied for *Xenopus* importin-α by size exclusion chromatography (39). The monomeric mouse importin-α, however, must use alternative regulatory mechanisms. Secondly, our results support the interpretation of the x-ray diffraction data of an intramolecular autoinhibitory interaction formed by the N-terminal sequence of the protein; previously, the possibility of the autoinhibitory sequence forming intermolecular interactions could not formally be discounted, because the path of the residues 55–69 was not visible in the electron density maps (14, 40). Finally, under our conditions, we observed little evidence of importin-α aggregation previously reported (41).

Our analysis of the importin-α/β binding is consistent with the previous estimates of the affinity of the two proteins in the range of 2–18 nM (21, 42, 43). The complex kinetic behavior observed with either ligand immobilized is consistent with the structural properties of the interaction. The IBB domain of importin-α has been shown to be necessary and sufficient for importin-β binding (7, 8). In the absence of importin-β, the IBB domain is mobile, with the exception of the sequence 44–54, which is bound to the Arm repeat domain of importin-α in an extended conformation (14). Importin-β therefore needs to sequester the sequence from importin-α and induce a helical conformation for a large part of the sequence (36, 37). This complex sequence of events is reflected in the complex kinetic behavior.

NLS Binding by Importin—The binding of NLSs to importin has previously been quantitated in a few cases (3). An ELISA-based assay was used to estimate the affinities of a few NLSs for mouse, yeast, and *Arabidopsis thaliana* importins, with the numbers ranging from 2 to 300 nM (3, 17–19, 21, 44). For mouse and yeast importins, the presence of importin-β increased the affinity in most cases by an order of magnitude when compared with importin-α alone. Using fluorescence depolarization, the dissociation constant for T-Ag NLS-green fluorescent protein binding to the truncated yeast importin-α lacking the IBB domain was estimated as 10 nM; the presence of importin-β increased the affinity of full-length importin-α (the dissociation constant changed from >10 μM to 33 nM) (45). Very recently, the same methodology was used to study the binding of full-length and truncated importin-α to c-Myc and T-Ag NLS mutants (46).

Our biosensor experiments show apparent affinities of a similar order of magnitude for NLS-importin binding and additionally provide information on the association and dissociation rates. The association rates appear to be in the range typically observed for biomolecules, consistent with the dynamic process of nuclear import and the nature of NLSs, which would be expected to be accessible for binding on the surface of proteins. Two general observations can be made. Firstly, representative monopartite and bipartite NLS bind with similar affinities. This can be explained by the crystal structures of Impα(70–529) bound to T-Ag and nucleoplasmin NLS peptides (13). Although the nucleoplasmin NLS spans both the major and minor NLS-binding sites of importin-α and buries a larger surface than the monopartite T-Ag NLS, the T-Ag NLS forms more favorable contacts in the major binding site, thus effectively yielding a similar affinity. Secondly, the N-terminally truncated protein Impα(70–529) binds to the NLS with an affinity similar to that of the importin-α/β complex. Importantly, this suggests that importin-β binding to importin-α creates an NLS-binding site in the complex that resembles the binding site in the truncated importin-α and that importin-β is unlikely to be directly involved in NLS binding.

Autoregulation of Importin-α during Nuclear Import—Our results provide support for the regulatory model of nuclear import proposed on the basis of the crystal structure of mouse importin-α (14) (Fig. 7). This model predicted a high affinity form (for NLS binding) of importin-α in the cytoplasm and an autoinhibited low affinity form in the nucleus (to prevent the binding of nuclear proteins and allow importin-α to return to the cytoplasm without the cargo). Ample evidence now exists to support this regulatory model. Very recently, it has been shown by fluorescence depolarization that yeast importin-α lacking the N-terminal 87 residues binds to NLS with ~10 nM affinity, but no measurable binding is observed with the full-length protein (45, 46). Our results using the biosensor similarly show no detectable binding between full-length importin-α and the

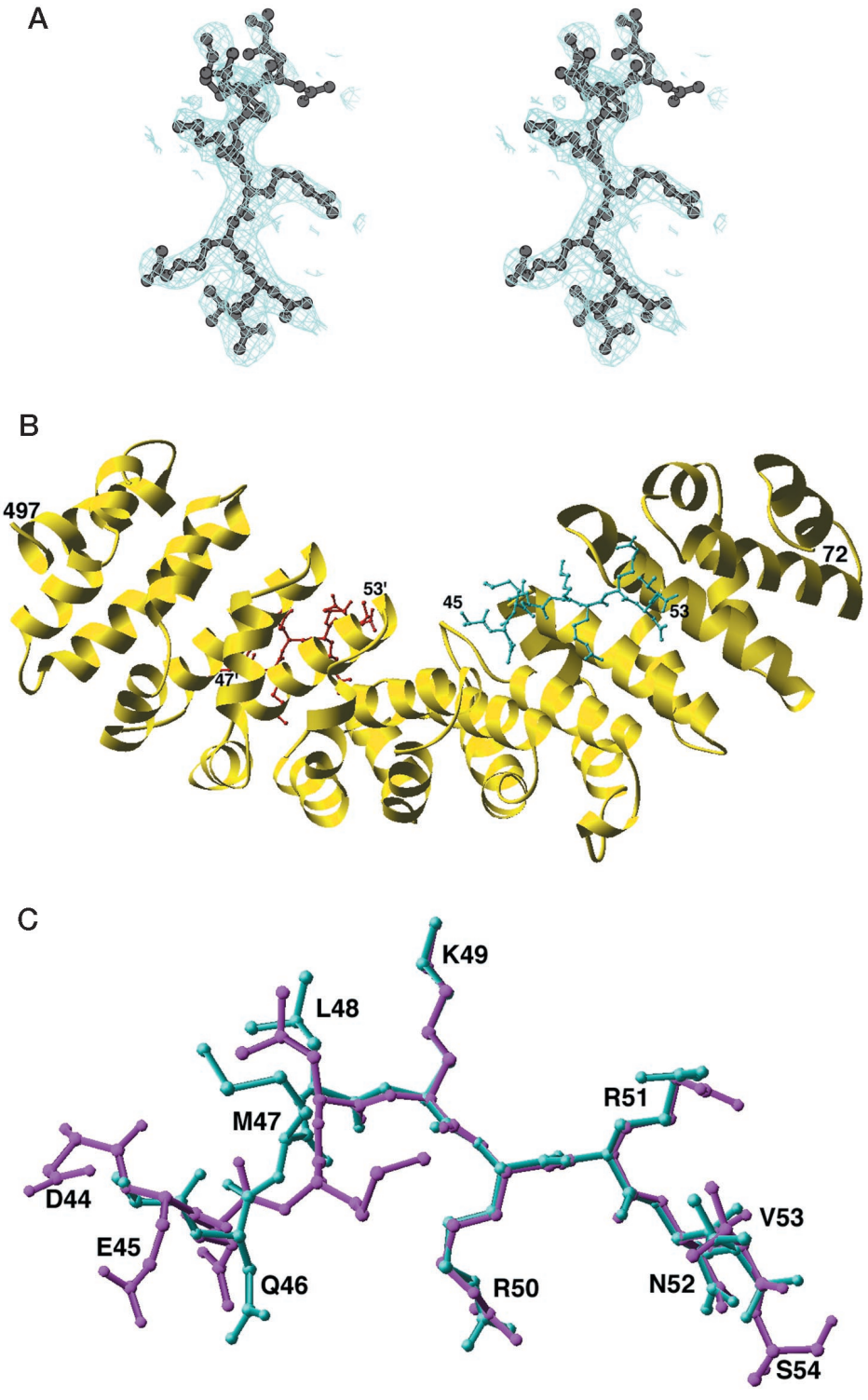

FIG. 5. **Crystal structure of the complex between Impα(44–54) and Impα(70–529).** *A*, stereoview of the electron density (drawn with the program BOBSCRIPT (52)) in the region of the peptide bound to the major binding site of Impα(70–529). All peptide residues were omitted from the model and simulated annealing run with the starting temperature of 1000 K. The electron density map was calculated with coefficients $3|F_{obs}| - 2|F_{calc}|$ and data between 30 and 2.8 Å resolution and contoured at 1.3 standard deviations. Superimposed is the refined model of the peptide. *B*, schematic diagram of the complex. Importin-α is shown as a *ribbon diagram* (*yellow*; drawn with program RIBBONS (53)). The superhelical axis of the repetitive part of the molecule is approximately horizontal. The two peptides are shown in a *ball-and-stick* representation; the peptide bound to the major site is colored *cyan*, and the peptide bound to the minor site is colored *red*. *C*, superposition of the Impα(44–54) peptide (*cyan*) and the corresponding region of full-length importin α (*magenta*) bound to the major NLS-binding site of importin-α. The Cα atoms of residues 70–496 were used in the superposition (drawn with the program RIBBONS (53)).

NLSs (the detection range is expected to be $\sim 10^3$–10^6 M^{-1} s^{-1} for k_a, 10^{-5}–10^{-1} s^{-1} for k_d). The structure of importin-β bound to a peptide from the IBB domain of importin-α (36) shows that importin-β binding should be able to sequester the autoinhibitory domain from the NLS binding site, thus activating the receptor. The results presented here now provide a system where essentially every step in the intrasteric regulatory pathway (15) has been quantitatively characterized.

In our system, importin-α and importin-β bind with ~11 nM affinity; previous ELISA-based estimations indicated affinities of 2–20 nM (21). The interaction involves mainly the IBB domain of importin-α, with little or no contribution from the rest of the protein. The importin-α/β complex binds functional monopartite and bipartite NLSs with ~40 nM affinities. After translocation of the heterotrimeric complex to the nuclear side, Ran-GTP binds to importin-β and can displace importin-α because its affinity is higher by an order of magnitude (0.8 nM) (47). On its own, importin-α has very low affinity (>10 μM) for NLSs, presumably to prevent binding nuclear proteins in the nucleus.

The key molecular event in this regulatory pathway is the transition of the autoregulatory IBB domain from the autoinhibitory interactions within importin-α (required in the

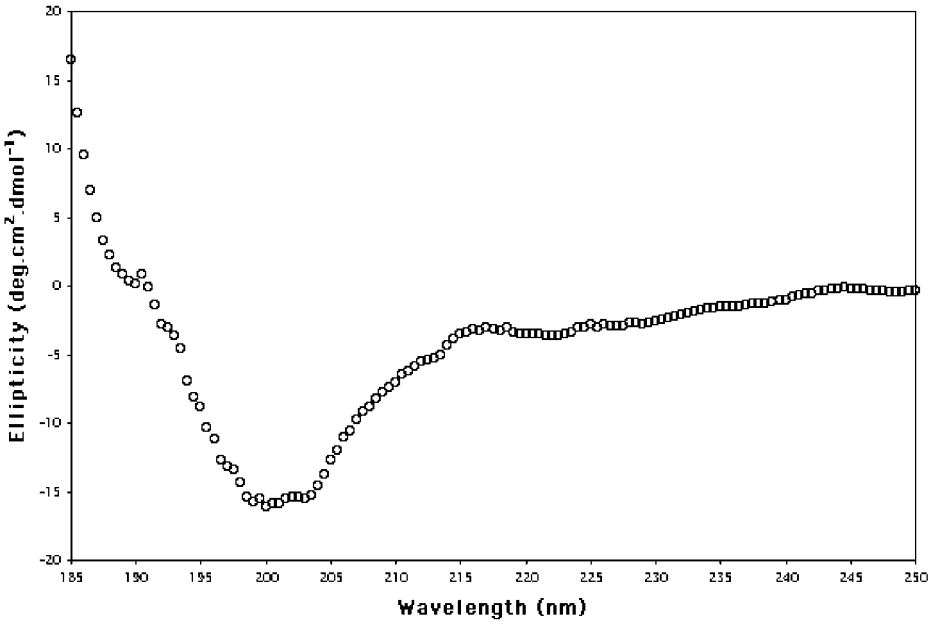

FIG. 6. **Circular dichroism analysis of the IBB domain.** The spectrum was recorded at pH 7 and 25 °C with a protein concentration of 1.08 mg ml^{-1}. The spectra were corrected with a base line obtained using buffer alone under the same conditions.

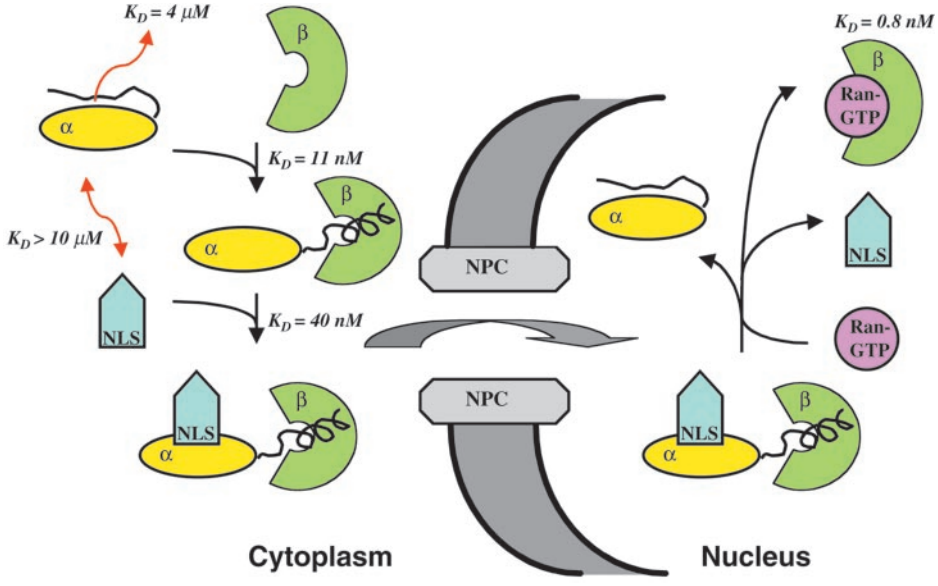

FIG. 7. **Schematic diagram of the NLS-dependent nuclear import pathway.** *Yellow*, importin-α; *green*, importin-β; *cyan*, NLS-containing cargo protein; *magenta*, Ran-GTP. For simplicity, other factors involved in the pathway such as nuclear transport factor-2, the nuclear export receptor for importin-α, and Ran-binding proteins have been omitted from the diagram. Dissociation constants for the different binding events are shown.

nucleus) to the interaction with importin-β (required in the cytoplasm). The IBB domain has little secondary structure propensity on its own (this work and Ref. 37). In the context of importin-α, it is largely mobile with the exception of the sequence 44–54, which binds to the Arm repeat region of importin-α (14). Our crystal structure of the complex of Impα(70–529) with a peptide corresponding to the autoinhibitory sequence 44–54 confirms the interpretation of the interactions in the native protein. This autoinhibitory binding resembles NLS binding to the major NLS binding site, and the sequence is bound in an extended fashion. By contrast, the sequence 11–54 interacting with importin-β adopts a helical conformation in the region 23–51 (36). Our results show that full-length importin-α or the IBB domain alone have similar affinities for importin-β (11 nM for importin-α/importin-β and 7 nM for IBB domain/importin-β). This may initially appear surprising, because in the case of full-length importin-α, the autoinhibitory contacts of the IBB domain need to be broken before the interaction can take place. Nevertheless, we show that the affinity of the IBB domain for the Arm repeat region of importin-α is quite weak, about 2 orders of magnitude lower than the importin-α/β interaction. The IBB domain-Arm repeat region interaction is similarly weaker than the interaction of NLSs with importin-α/β complex. However, our measurements neglect the effect of the local concentration of the IBB domain; within importin-α, the IBB domain is tethered to the protein and is therefore present in a very high effective local concentration. This explanation is also consistent with the reduction in affinity for NLSs of at least 3 orders of magnitude in the autoinhibited form of importin-α, when compared with the importin-α/β complex. Hodel *et al.* (46) have recently estimated the energy of autoinhibition as 3 kcal mol^{-1}. The difference in affinities of the autoinhibitory domain and the NLSs with the Arm repeat region of importin-α is consistent with the structural results (13, 14); the favorable interactions are much better exploited in the NLS peptides, which contain a larger number of positively charged residues in the basic cluster.

Our biosensor experiments did not detect any binding of full-length importin-α to either a representative monopartite and bipartite NLS. This is in agreement with the fluorescence depolarization experiments using yeast importin-α (45, 46). However, several reports show evidence of high affinity binding

of NLSs to full-length importin-α in the absence of importin-β. For example, the affinities of T-Ag NLS and the NLS of the cytoskeletal red cell protein 4.1 to human importin-α isoform Rch1 were estimated to be 56 and 30 nM, respectively, using a resonant mirror detection technique (43). Similarly, importin-β had little effect on the affinities of *A. thaliana* importin-α for T-Ag and N1N2 NLSs (8.3 and 6.7 nM, respectively) (21). One possible explanation is that the particular isoforms of importin-α used in these studies may have different regulatory mechanisms. However, much smaller differences in affinity were also observed with mouse and yeast importin-α using the ELISA-based assay (17–19, 44). For example, the affinity of an extended T-Ag NLS was measured as 5.5 and 2.7 nM for mouse importin-α and importin-α/β complex, respectively, and 2.0 and 2.1 nM for yeast importin-α and importin-α/β complex, respectively (19). We have previously shown (and will show in a future publication)[2] that the residues N-terminal to the NLS, including protein kinase CK2 and double-stranded DNA-dependent protein kinase phosphorylation sites, increase the NLS binding affinity by at least an order of magnitude (18, 48, 49), so that one can speculate that the presence of these residues may indeed be able to compete, albeit inefficiently, with the IBB domain for the NLS binding site in importin-α even in the absence of importin-β. It can also not be excluded that the weak autoinhibitory interactions may be partially disrupted in the conditions used in the ELISA.

Conclusions—Our results presented here endorse the regulatory model of nuclear import proposed previously on the basis of structural information (14) and provide a quantitative description of essentially every binding and regulatory step in the intrasteric regulatory pathway. A schematic model of nuclear import summarizing the available data is illustrated in Fig. 7. Cytoplasmic importin-β binding to the IBB domain of importin-α ($K_D \sim 11$ nM) removes the autoinhibitory segment from the NLS-binding site, rendering importin-α/β active for binding an NLS-containing protein ($K_D = \sim 40$ nM). After translocation through the nuclear pore complex into the nucleus, Ran-GTP binding to importin-β ($K_D = 0.8$ nM) causes the dissociation of importin-β from importin-α and cargo release into the nucleoplasm. The cargo cannot bind to the autoinhibited importin-α ($K_D = >10$ μM); although the affinity of the autoinhibitory segment for the Arm repeat domain of importin α is only ~4 μM, the autoinhibition is potent because of the high local concentration of the autoinhibitory segment. The autoinhibitory segment changes conformation from extended when bound to importin-α, to helical when bound to importin-β and has little secondary structure on its own. Similarly, importin-β conformationally adapts to its binding partners (36, 37, 50, 51). The remarkable molecular choreography of nuclear import is likely representative of many other intrasteric regulatory mechanisms (15).

Acknowledgment—We thank Ben Attcliffe (University of Melbourne) for assistance with circular dichroism spectroscopy.

REFERENCES

1. Dingwall, C., and Laskey, R. A. (1991) *Trends Biochem. Sci.* **16,** 478–481
2. Christophe, D., Christophe-Hobertus, C., and Pichon, B. (2000) *Cell. Signal.* **12,** 337–341
3. Jans, D. A., Xiao, C. Y., and Lam, M. H. (2000) *Bioessays* **22,** 532–544
4. Sweitzer, T. D., Love, D. C., and Hanover, J. A. (2000) *Curr. Top. Cell Regul.* **36,** 77–94
5. Wente, S. R. (2000) *Science* **288,** 1374–1377
6. Yoneda, Y. (2000) *Genes Cells* **5,** 777–787
7. Gorlich, D., Henklein, P., Laskey, R. A., and Hartmann, E. (1996) *EMBO J.* **15,** 1810–1817
8. Weis, K., Ryder, U., and Lamond, A. I. (1996) *EMBO J.* **15,** 1818–1825
9. Moroianu, J., Blobel, G., and Radu, A. (1996) *Proc. Natl. Acad. Sci. U. S. A.* **93,** 6572–6576
10. Peifer, M., Berg, S., and Reynolds, A. B. (1996) *Cell* **76,** 789–791
11. Conti, E., Uy, M., Leighton, L., Blobel, G., and Kuriyan, J. (1998) *Cell* **94,** 193–204
12. Conti, E., and Kuriyan, J. (2000) *Structure* **8,** 329–338
13. Fontes, M. R. M., Teh, T., and Kobe, B. (2000) *J. Mol. Biol.* **297,** 1183–1194
14. Kobe, B. (1999) *Nat. Struct. Biol.* **6,** 388–397
15. Kobe, B., and Kemp, B. E. (1999) *Nature* **402,** 373–376
16. Rexach, M., and Blobel, G. (1995) *Cell* **83,** 683–692
17. Efthymiadis, A., Shao, H., Hubner, S., and Jans, D. A. (1997) *J. Biol. Chem.* **272,** 22134–22139
18. Hubner, S., Xiao, C. Y., and Jans, D. A. (1997) *J. Biol. Chem.* **272,** 17191–17195
19. Briggs, L. J., Stein, D., Goltz, J., Corrigan, V. C., Efthymiadis, A., Hubner, S., and Jans, D. A. (1998) *J. Biol. Chem.* **273,** 22745–22752
20. Kussel, P., and Frasch, M. (1995) *Mol. Gen. Genet.* **248,** 351–363
21. Hubner, S., Smith, H. M. S., Hu, W., Chen, C. K., Rihs, H. P., Paschal, B. M., Raikhel, N. V., and Jans, D. A. (1999) *J. Biol. Chem.* **274,** 22610–22617
22. Chi, N. C., Adam, E. J., Visser, G. D., and Adam, S. A. (1996) *J. Cell Biol.* **135,** 559–569
23. Imamoto, N., Shimamoto, T., Takao, T., Tachibana, T., Kose, S., Matsubae, M., Sekimoto, T., Shimonishi, Y., and Yoneda, Y. (1995) *EMBO J.* **14,** 3617–3626
24. Michell, B. J., Stapleton, D., Mitchelhill, K. I., House, C. M., Katsis, F., Witters, L. A., and Kemp, B. E. (1996) *J. Biol. Chem.* **271,** 28445–28450
25. Catimel, B., Ritter, G., Welt, S., Old, L. J., Cohen, L., Nerrie, M. A., White, S. J., Heath, J. K., Demediuk, B., Domagala, T., Lee, F. T., Scott, A. M., Tu, G. F., Ji, H., Moritz, R. L., Simpson, R. J., Burgess, A. W., and Nice, E. C. (1996) *J. Biol. Chem.* **271,** 25664–25670
26. Fridman, M., Walker, F., Catimel, B., Domagala, T., Nice, E., and Burgess, A. (2000) *Biochemistry* **39,** 15603–15611
27. Mathieu, M. N., Wade, J. D., Tregear, G. W., Bond, C. P., Summers, R. J., Catimel, B., Nice, E. C., and Otvos, L. (2001) *J. Pept. Res.* **57,** 374–382
28. Nice, E. C., and Catimel, B. (1999) *Bioessays* **21,** 339–352
29. Otwinowski, Z., and Minor, W. (1997) *Methods Enzymol.* **276,** 307–326
30. Brünger, A. T., Adams, P. D., Clore, G. M., DeLano, W. L., Gros, P., Grosse-Kunstleve, R. W., Jiang, J. S., Kuszewski, J., Nilges, M., Pannu, N. S., Read, R. J., Rice, L. M., Simonson, T., and Warren, G. L. (1998) *Acta Crystallogr. Sect. D Biol. Crystallogr.* **54,** 905–921
31. Brünger, A. T. (1992) *Nature* **355,** 472–475
32. Jones, T. A., Bergdoll, M., and Kjeldgaard, M. (1990) in *Crystallographic and Modeling Methods in Molecular Design* (Bugg, C. E., and Ealick, S. E., eds) pp. 189–195, Springer-Verlag, New York
33. Laskowski, R. A., MacArthur, M. W., Moss, D. S., and Thornton, J. M. (1993) *J. Appl. Crystallogr.* **26,** 283–291
34. CCP4 (1994) *Acta Crystallogr. Sect. D Biol. Crystallogr.* **50,** 760–763
35. Stenberg, E., Persson, B., Roos, H., and Urbaniczki, J. (1990) *J. Colloid Interface* **43,** 513–526
36. Cingolani, G., Petosa, C., Weis, K., and Muller, C. W. (1999) *Nature* **399,** 221–229
37. Cingolani, G., Lashuel, H. A., Gerace, L., and Muller, C. W. (2000) *FEBS Lett.* **484,** 291–298
38. Imamoto, N., Shimamoto, T., Kose, S., Takao, T., Tachibana, T., Matsubae, M., Sekimoto, T., Shimonishi, Y., and Yoneda, Y. (1995) *FEBS Lett.* **368,** 415–419
39. Gorlich, D., Prehn, S., Laskey, R. A., and Hartmann, E. (1994) *Cell* **79,** 767–778
40. Stewart, M., and Rhodes, D. (1999) *Nat. Struct. Biol.* **6,** 301–304
41. Percipalle, P., Butler, P. J., Finch, J. T., Jans, D. A., and Rhodes, D. (1999) *J. Mol. Biol.* **292,** 263–273
42. Kohler, M., Speck, C., Christiansen, M., Bischoff, F. R., Prehn, S., Haller, H., Gorlich, D., and Hartmann, E. (1999) *Mol. Cell. Biol.* **19,** 7782–7791
43. Gascard, P., Nunomura, W., Lee, G., Walensky, L. D., Krauss, S. W., Takakuwa, Y., Chasis, J. A., Mohandas, N., and Conboy, J. G. (1999) *Mol. Biol. Cell* **10,** 1783–1798
44. Hu, W., and Jans, D. A. (1999) *J. Biol. Chem.* **274,** 15820–15827
45. Fanara, P., Hodel, M. R., Corbett, A. H., and Hodel, A. E. (2000) *J. Biol. Chem.* **275,** 21218–21223
46. Hodel, M. R., Corbett, A. H., and Hodel, A. E. (2001) *J. Biol. Chem.* **276,** 1317–1325
47. Gorlich, D., Dabrowski, M., Bischoff, F. R., Kutay, U., Bork, P., Hartmann, E., Prehn, S., and Izaurralde, E. (1997) *J. Cell Biol.* **138,** 65–80
48. Xiao, C. Y., Hubner, S., and Jans, D. A. (1997) *J. Biol. Chem.* **272,** 22191–22198
49. Xiao, C. Y., Jans, P., and Jans, D. A. (1998) *FEBS Lett.* **440,** 297–301
50. Vetter, I. R., Arndt, A., Kutay, U., Gorlich, D., and Wittinghofer, A. (1999) *Cell* **97,** 635–646
51. Lee, S. J., Imamoto, N., Sakai, H., Nakagawa, A., Kose, S., Koike, M., Yamamoto, M., Kumasaka, T., Yoneda, Y., and Tsukihara, T. (2000) *J. Mol. Biol.* **302,** 251–264
52. Esnouf, R. M. (1997) *J. Mol. Graphics* **15,** 133–138
53. Carson, M. (1997) *Methods Enzymol.* **277,** 493–505

[2] M. R. M. Fontes, T. Teh, G. Toth, A. John, I. Pavo, D. A. Jans, and B. Kobe, submitted for publication.

Biophysical Characterization of Interactions Involving Importin-α during Nuclear Import

Bruno Catimel, Trazel Teh, Marcos R. M. Fontes, Ian G. Jennings, David A. Jans, Geoffrey J. Howlett, Edouard C. Nice and Bostjan Kobe

J. Biol. Chem. 2001, 276:34189-34198.
doi: 10.1074/jbc.M103531200 originally published online July 11, 2001
